Development of the Yearly Mode-1 M_2 Internal Tide Model in 2019

ZHONGXIANG ZHAO[a]

[a] *Applied Physics Laboratory, University of Washington, Seattle, Washington*

(Manuscript received 26 August 2021, in final form 11 December 2021)

ABSTRACT: The yearly mode-1 M_2 internal tide model in 2019 is constructed using sea surface height measurements made by six concurrent satellite altimetry missions: *Jason-3*, *Sentinel-3A*, *Sentinel-3B*, *CryoSat-2*, *Haiyang-2A*, and *SARAL*/AltiKa. The model is developed following a three-step procedure consisting of two rounds of plane wave analysis with a spatial bandpass filter in between. Prior mesoscale correction is made on the altimeter data using AVISO gridded mesoscale fields. The model is labeled Y2019, because it represents the 1-yr-coherent internal tide field in 2019. In contrast, the model developed using altimeter data from 1992 to 2017 is labeled MY25, because it represents the multiyear-coherent internal tide field in 25 years. Thanks to the new mapping technique, model errors in Y2019 are as low as those in MY25. Evaluation using independent altimeter data confirms that Y2019 reduces slightly less variance (~6%) than MY25. Further analysis reveals that the altimeter data from five missions (without *Jason-3*) can yield an internal tide model of almost the same quality. Comparing Y2019 and MY25 shows that mode-1 M_2 internal tides are subject to significant interannual variability in both amplitude and phase, and their interannual variations are a function of location. Along southward internal tides from Amukta Pass, the energy flux in Y2019 is 2 times larger and the phase speed is about 1.1% faster. This mapping technique has been applied successfully to 2017 and 2018. This work demonstrates that yearly internal tides can be observed by concurrent altimetry missions and their interannual variations can be determined.

SIGNIFICANCE STATEMENT: This work is motivated to study the interannual variations of internal tides using observation-based yearly internal tide models from satellite altimetry. Previous satellite observations of internal tides are usually based on 25 years of altimeter data from 1993 to 2017. The yearly subsetted altimeter data are short, so that the resultant yearly models are overwhelmed by noise. A new mapping technique is developed and demonstrated in this paper. It paves a path to study the interannual and decadal variations of internal tides on a global scale and monitor the global ocean changes by tracking long-range internal tides.

KEYWORDS: Ocean; Internal waves; Topographic effects; Tides; Altimetry; Satellite observations

1. Introduction

Internal tides (internal waves of tide frequency) are ubiquitous in the global ocean, because of their numerous generation sites over topographic features and long-distance propagation in the open ocean (Ray and Mitchum 1996; Egbert and Ray 2000; Alford et al. 2007; Garrett and Kunze 2007; Arbic et al. 2012; Niwa and Hibiya 2014; de Lavergne et al. 2020; Kelly et al. 2021). Internal tides play an important role in a wide variety of ocean processes such as diapycnal mixing, mass transport, and meridional overturning circulation (Jayne and St. Laurent 2001; Rudnick et al. 2003; MacKinnon et al. 2017; Vic et al. 2019; Whalen et al. 2020). The generation and propagation of internal tides are modulated by time-varying ocean environment over time scales ranging from days to decades (Ray and Zaron 2011; Zaron and Egbert 2014; Zhou et al. 2015; Zhao 2016a,b; Buijsman et al. 2017; Zaron 2017; Löb et al. 2020; Zhao 2021). Satellite altimetry offers a unique technique for observing internal tides via their centimeter-scale sea surface fluctuations. However, it is a challenging task to map internal tides using satellite altimeter data, because 1) internal tides are of short wavelength (100–200 km) and thus require data from denser ground tracks to resolve them, and 2) internal tide signals are weak [1% of sea surface height (SSH) variance] and thus require more independent data to suppress noise. Therefore, previous internal tide models are usually constructed using merged altimeter data from multiple missions over many years (Dushaw 2015; Ray and Zaron 2016; Zhao et al. 2016; Zaron 2019; Zhao 2019). As a consequence, all these models represent multiyear-coherent internal tide fields. They all miss time-varying incoherent components (Carrere et al. 2021). One technical strategy addressing this issue is mapping internal tides in short time-windows, so that their temporal variations can be quantified by comparing a series of internal tide models. Based on this strategy, the author has constructed four seasonal internal tide models using seasonally subsetted altimeter data and studied their seasonal variations (Zhao 2021). The present paper explores the feasibility of developing yearly internal tide models using yearly subsetted satellite altimeter data. The ultimate goal is to study the interannual and decadal variations of internal tides. This paper focuses on the dominant mode-1 M_2 internal tides.

There are six satellite altimetry missions in operation in 2019 (section 2a). The merged altimeter data have sufficiently high spatial resolution for mapping short-scale internal tides. However, the challenge stems from the short six satellite years of data in 2019. Because mode-1 M_2 internal tides account for only 1% of the SSH variance (Zhao 2021), large model errors caused by the short data record would overwhelm the real

Corresponding author: Zhongxiang Zhao, zzhao@apl.uw.edu

DOI: 10.1175/JTECH-D-21-0116.1

TABLE 1. Information on six concurrent altimetry missions in 2019. The ground tracks of *Sentinel-3A* and *Sentinel-3B* are interleaved and double the spatial resolution. *SARAL*/AltiKa is along a loosely controlled drifting orbit; therefore, it has variable intertrack intervals.

Mission	Orbit	Repeat period (days)	No. of tracks	Track interval (km)
Jason-3	Exact-repeat track	9.9156	254	315
Sentinel-3A	Exact-repeat track	27	770	100
Sentinel-3B	Exact-repeat track	27	770	100
CryoSat-2	Long-repeat track	369	10 688	7.5
Haiyang-2A	Geodetic track	168	4630	17.3
SARAL/AltiKa	Drifting track	35	1002	~80

internal tide signals. In this paper, a new mapping technique is brought up to address this challenge. Its core methods are two rounds of plane wave analysis with a spatial bandpass filter in between (Zhao 2019, 2020, 2021). Prior to plane wave analysis, mesoscale correction is made on the altimeter data using Archiving, Validation, and Interpretation of Satellite Oceanographic Data (AVISO) gridded mesoscale fields (Ray and Byrne 2010; Ray and Zaron 2016; Pujol et al. 2016). The combination gives a new mapping technique, and makes it possible to construct yearly mode-1 M_2 internal tide models. Previously, the author has shown that yearly mode-1 M_2 internal tides can be extracted along strong internal tidal beams (Zhao 2016a). Fortunately, the new mapping technique can extract mode-1 M_2 internal tides throughout the global ocean. The resultant internal tide model proves reliable. Significant interannual variations in both amplitude and phase are observed by comparing the 1-yr-coherent model and the previous 25-yr-coherent model (Zhao 2019).

The rest of this paper is as follows. Section 2 describes satellite altimeter data and the new mapping technique. Section 3 presents the resultant internal tide model, and evaluates the model using independent altimeter data. Section 4 examines internal tide models developed using three and five altimetry missions, respectively. Section 5 demonstrates the interannual variability of internal tides revealed by these models. Section 6 shows that this technique has been applied successfully to 2017 and 2018. Section 7 is a summary.

2. Data and methods

a. Satellite altimeter data

The satellite altimeter data in 2019 are from six concurrent altimetry missions. They are *Jason-3*, *Sentinel-3A*, *Sentinel-3B*, *CryoSat-2*, *Haiyang-2A*, and *SARAL*/AltiKa. Among them, the first three missions are along exact-repeat tracks, and the last three missions are along nonrepeat tracks. All missions have SSH measurements in multiple years, but their data are trimmed to 2019 to construct yearly internal tide models. Table 1 lists their different orbit configurations. Figure 1 shows their ground tracks around Hawaii. *Jason-3* has a repeat period of 9.9156 days and 254 ground tracks. It has the highest temporal resolution and lowest spatial resolution among these missions (Fig. 1a). *Sentinel-3A* and *Sentinel-3B* are identical. They each have a repeat period of 27 days and 770 ground tracks. Their interleaved ground tracks double the spatial resolution (Fig. 1b). *CryoSat-2* has a long repeat period of 369 days and samples the ocean along 10 668 ground tracks (Wingham et al. 2006). *CryoSat-2* has the densest ground tracks of all altimetry missions (Fig. 1c). At the equator, its intertrack spacing is only 7.5 km. *Haiyang-2A* is in its geodetic phase in 2019. It has a repeat cycle of 168 days and makes 4630 ground tracks in one cycle (Kong et al. 2019). *SARAL*/AltiKa is in its drifting orbit phase in 2019 (Dibarboure et al. 2018). It has a repeat period of 35 days and 1002 ground tracks per cycle (same as in its normal phase), but its orbit is loosely controlled (Fig. 1e). The merged data from the six missions have a large number of ground tracks and high spatial resolution for mapping internal tides (Fig. 1f). However, the merged data are only six satellite years long. The resultant model is labeled Y2019, because it represents the 1-yr-coherent internal tide field in 2019.

b. Mesoscale correction

Mesoscale correction is needed to construct low-noise-level internal tide models. Otherwise, direct mapping internal tides using the raw altimeter data would yield internal tides with large errors (examined separately, not shown). In this study, prior mesoscale correction is made on the altimeter data using AVISO gridded mesoscale fields. Mesoscale correction is brought up to suppress mesoscale signals by Ray and Byrne (2010) and has been employed in mapping internal tides by Ray and Zaron (2016) and Zaron (2019). Ray and Zaron (2016) make mesoscale correction before pointwise harmonic analysis. Zaron (2019) makes mesoscale correction before polynomial fits of propagating internal tides. In this study, mesoscale correction will be combined with plane wave analysis and spatial bandpass filtering.

The AVISO mesoscale fields are constructed by objective analysis of multisatellite altimetry along-track data (Pujol et al. 2016). The fields are gridded daily in time and 0.25° longitude × 0.25° latitude in the horizontal. The AVISO data are downloaded from the Copernicus Marine Environment Monitoring Service (CMEMS) website. A known issue with mesoscale correction is that the AVISO SSH fields may contain leaked internal tide signals. Therefore, subtracting the AVISO fields may remove and underestimate internal tides. To address this issue, the AVISO mesoscale fields are 2D low-pass filtered with a cutoff wavelength of 200 km following Zaron and Ray (2018). The cutoff wavelength of 200 km is chosen to be just greater than wavelengths of mode-1 M_2 internal tides (100–200 km). The 2D low-pass filter removes internal tide

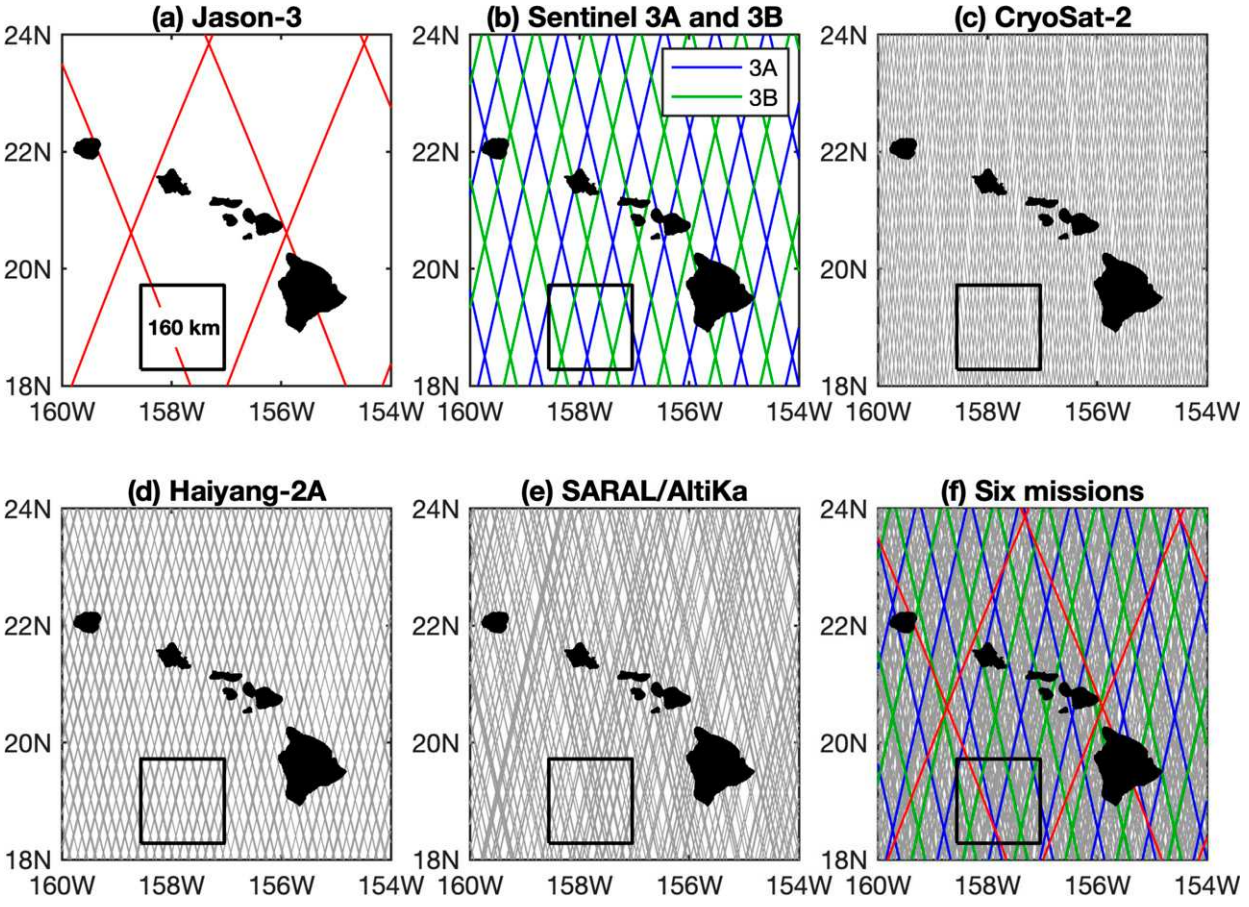

FIG. 1. Ground tracks of six concurrent altimetry missions in 2019: (a) *Jason-3*, (b) *Sentinel-3A* and *Sentinel-3B*, (c) *CryoSat-2*, (d) *Haiyang-2A*, (e) *SARAL*/AltiKa, and (f) all six altimetry missions. *Jason-3*, *Sentinel-3A*, and *Sentinel-3B* are exact-repeat missions. *CryoSat-2*, *Haiyang-2A*, and *SARAL*/AltiKa are nonrepeat missions. Black boxes indicate the 160 km × 160 km fitting window used in this study.

signals in the AVISO mesoscale fields. Afterward, mesoscale correction is made on the altimeter data using the low-pass filtered mesoscale fields.

An alternative method for suppressing nontidal noise is using an along-track high-pass filter (Zhao 2019). In this study, the yearly internal tide model is also constructed using the along-track high-pass filtered data. This study uses a fourth-order Butterworth high-pass filter with cutoff wavelength of 500 km. The resultant internal tide model is labeled Y2019test. Y2019test and Y2019 are constructed using the same data and the same mapping parameters, except for different preprocess methods: mesoscale correction versus along-track filtering (Table 2). However, the along-track high-pass filter removes internal tides having large angles with

TABLE 2. Internal tide models Y2019, Y2019test and MY25 are constructed using different altimeter datasets or different preprocess methods. MY25 is constructed and labeled Zhao19 in Zhao (2019).

Model	Y2019 (Y2019test)	MY25
Time coverage	2019	1993–2017
Altimetry missions	*Jason-3*, *Sentinel-3A*, *Sentinel-3B*, *CryoSat-2*, *Haiyang-2A*, *SARAL*/AltiKa	TOPEX/Poseidon, *Jason-1*/*-2*/*-3*, *ERS-2*, *Envisat*, *Geosat Follow-On*
Data record	6 satellite years	54 satellite years
Preprocess	Mesoscale correction (along-track high-pass filter)	No filter
Step 1	Plane wave analysis: 0.2° lon × 0.2° lat, 160 km × 160 km, 5 waves	
Step 2	Spatial bandpass filter: 850 × 850 km, [0.8 1.25] × K(lon, lat)	
Step 3	Plane wave analysis: 0.2° lon × 0.2° lat; 160 km ×160 km; 5 waves	

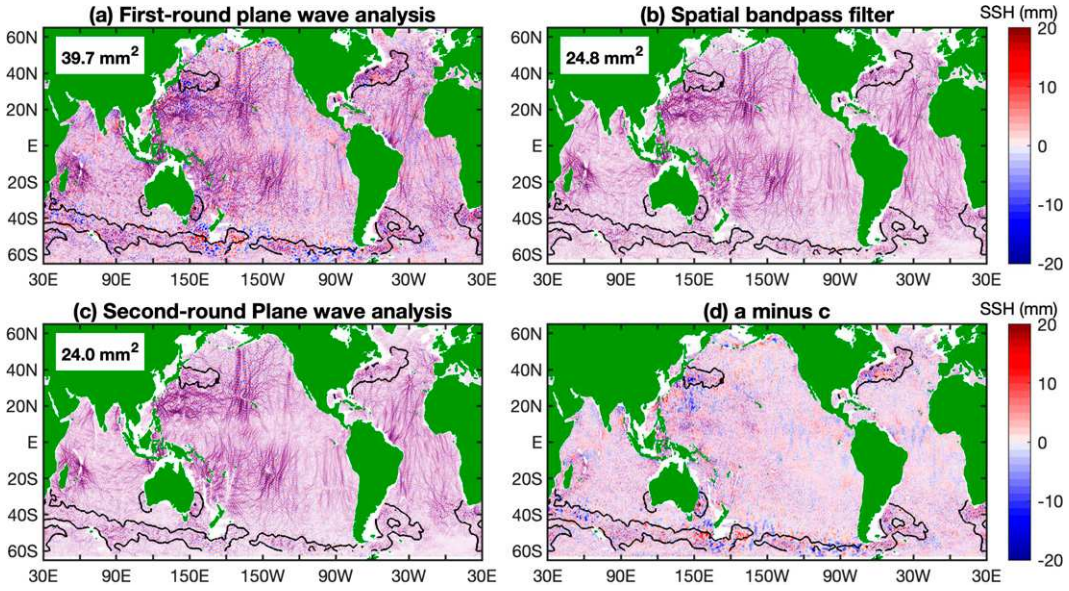

FIG. 2. Mapping procedure. Mode-1 M_2 internal tides are mapped using altimeter data preprocessed by mesoscale correction (Y2019). (a) Internal tides obtained by the first-round plane wave analysis. (b) Internal tides cleaned by spatial bandpass filtering. (c) Internal tides obtained by the second-round plane wave analysis. (d) The difference between (a) and (c). Black contours indicate regions of strong currents. Numbers are global mean SSH variances (excluding regions of strong currents).

respect to satellite ground tracks and suppresses west–east propagating internal tides, because the satellite ground tracks are generally in the south–north direction. Therefore, Y2019test and Y2019 have almost the same southward and northward components. But Y2019test underestimates the eastward and westward internal tides (section 3).

c. *Internal tide model MY25*

The internal tide model Y2019 will be evaluated using the 25-yr-coherent model constructed using 25 years of satellite altimeter data from 1993 to 2017 (Zhao 2019). This model is labeled MY25, because it represents the multiyear-coherent field in 25 years. The seven altimetry missions used for MY25 all are exact-repeat missions: TOPEX/Poseidon, *Jason-1*, *Jason-2*, *Jason-3*, *ERS-2*, *Envisat*, and *Geosat Follow-On* (*GFO*). There are a total of 54 satellite years of altimeter data. The data size is large enough to successfully suppress noise; therefore, prior mesoscale correction is not necessary (Zhao 2019). Y2019 and MY25 are constructed following the same procedure and using the same mapping parameters (Table 2). In this paper, they are compared for the following reasons: 1) to validate the newly developed internal tide model Y2019, and 2) to examine the interannual variations of mode-1 M_2 internal tides.

d. *Mapping procedure*

Mode-1 M_2 internal tides are extracted following a three-step mapping technique developed by the author (Zhao 2019). An interested reader is referred to that work for more details. Pointwise harmonic analysis is not used in this procedure, because the SSH time series from nonrepeat missions at any given point are too short to do harmonic analysis. Figure 2 gives one example showing the intermediate internal tide fields obtained in each of the three steps.

1) STEP 1: FIRST-ROUND PLANE WAVE ANALYSIS

Mode-1 M_2 internal tides are mapped by plane wave analysis from discrete satellite ground tracks (Fig. 1). The data have been processed by mesoscale correction (Y2019) or along-track high-pass filtering (Y2019test). Plane wave analysis extracts internal tides from satellite altimeter data by fitting plane waves using all measurements in one given fitting window. Amplitudes, phases, and propagation directions of target internal tidal waves are determined by least squares fits in overlapping fitting windows. The period and wavenumber of the target waves are two prerequisite parameters. The M_2 tidal period is 12.4206 h. Its first-mode baroclinic wavenumbers are calculated using hydrographic profiles in the *World Ocean Atlas* (*WOA*) *2013* (Locarnini et al. 2013; Zweng et al. 2013). The calculation methods have been described in previous studies (Kelly 2016; Zhao et al. 2016). An iterative algorithm has been developed to extract an arbitrary number of waves in the order of decreasing amplitude. The size of fitting windows is chosen to be 160 km × 160 km (Table 2). Plane wave analysis is conducted on a regular grid of 0.2° longitude × 0.2° latitude. At each grid point, the largest five mode-1 M_2 internal tidal waves are determined one by one, and their sum gives the M_2 internal tide solution at this point.

2) STEP 2: SPATIAL BANDPASS FILTER

A horizontal 2D spatial bandpass filter is employed to remove nontidal noise and higher baroclinic modes. Taking

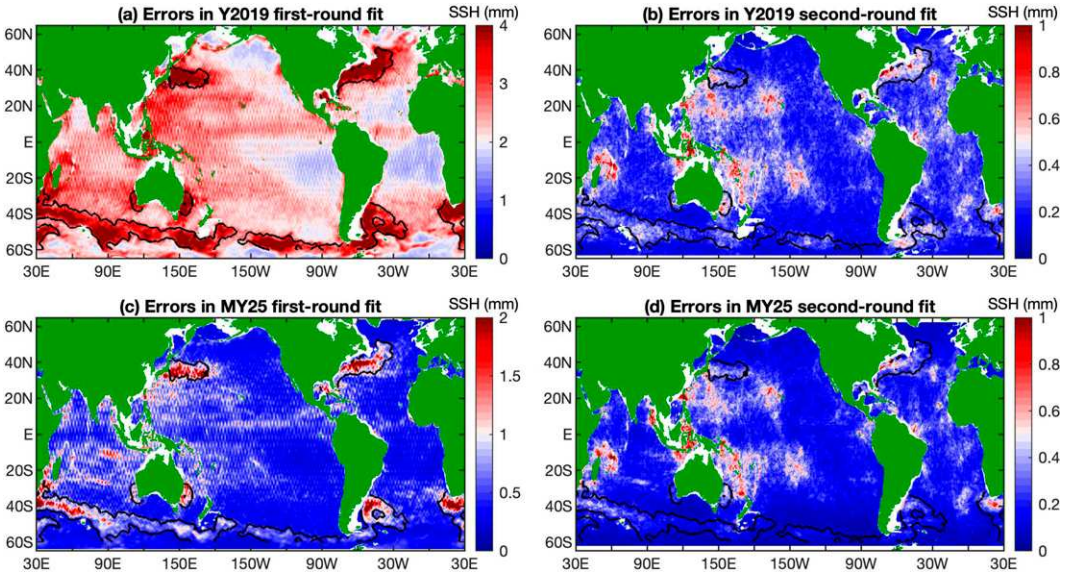

FIG. 3. Model errors are indicated by the 95% confidence intervals in plane wave analysis. Model errors in both Y2019 and MY25 are shown. (a) Y2019 first-round fit. (b) Y2019 second-round fit. (c) MY25 first-round fit. (d) MY25 second-round fit. Black contours indicate regions of strong currents. Note that different colormap ranges are used to avoid color saturation.

advantage of the spatially regular model obtained in step 1, M_2 internal tides can be cleaned by removing components that do not meet the wavenumber requirement. The filter is applied to a number of overlapping windows of 850 km × 850 km. The internal tide field in each window is first converted to the 2D wavenumber spectrum $S(k)$ by Fourier transform. Then $S(k)$ is truncated to [0.8 1.25] × K(lon, lat) using the local theoretical wavenumber. In the end, the truncated $S(k)$ is converted back to the internal tide field by inverse Fourier transform.

3) STEP 3: SECOND-ROUND PLANE WAVE ANALYSIS

Plane wave analysis can separate internal tide waves of different propagation directions. In this step, plane wave analysis is employed to decompose the total internal tide field into multiple internal waves of different propagation directions. The same parameters as in step 1 are used in the decomposition. Five waves are determined and saved separately with their amplitudes, phases, and propagation directions. The decomposed internal tide components will be used to study their along-beam propagation and energetics (section 5d). The multiwave decomposition works well in the open ocean; however, it may be problematic in complex internal tide fields such as the source regions (Zaron 2019; Zhao et al. 2019). In one source region, the internal tide field would better be decomposed into more than five waves and conducted in smaller windows. Alternatively, Zaron (2019) constructs internal tide fields with spatially variable amplitudes and phases using high-order polynomial fits.

e. *Intermediate results*

Figure 2 shows the intermediate mode-1 M_2 internal tide fields obtained in mapping Y2019. Figure 2a shows the field obtained in the first-round plane wave analysis. Internal tides can be clearly seen, but noise is high. It may overwhelm internal tides in some regions. Its global mean variance is 39.7 mm^2. Figure 2b shows the bandpass filtered internal tide field. Its global mean variance is 24.8 mm^2. It means that the bandpass filter removes 14.9 mm^2 variance, which is about 40% of the original variance (Fig. 2a). Figure 2c shows the internal tide field obtained in the second-round plane wave analysis. In this step, the global mean variance decreases from 24.8 to 24.0 mm^2 or by 3%, indicating that the second-round plane wave analysis does not reduce much noise. Its main goal is to decompose the total field into five waves at each grid point. Figure 2c is the final internal tide field. For comparison, Fig. 2d shows the difference between the first-round and second-round plane wave analysis, indicating that nontidal noise is removed throughout the ocean. As explained above, the cleaning is mostly caused by the spatial bandpass filter in step 2. This example illustrates the three-step mapping procedure, and highlights the importance of spatial bandpass filter (step 2) in constructing internal tide models.

f. *Model errors*

In plane wave analysis, the 95% confidence intervals are calculated in MATLAB's built-in regression function using the standard formula for Gaussian distributed data. They are used to check model errors in the mapping technique. Figures 3a and 3b show model errors in the two rounds of plane wave analysis, respectively. In the first-round fit, model errors are usually larger than 2 mm, and may be up to 4 mm. In the second-round fit, model errors are generally lower than 0.5 mm. But in regions of strong generation sites (e.g., the Hawaiian Ridge), model errors may be up to 1 mm. The decrease in model errors is

attributed to the spatial bandpass filter in step 2, which significantly suppresses nontidal noise. Figure 3a has an obvious spatial pattern in model errors, which is caused by the inhomogeneous distribution of satellite ground tracks (Fig. 1).

For comparison, Figs. 3c and 3d show model errors in MY25 in the two rounds of plane wave analysis, respectively. Figure 3c has a similar spatial pattern to Fig. 3a caused by discrete satellite ground tracks. Figure 3c shows that MY25 has much lower model errors, due to its 54 satellite years of data. Interestingly, in the second-round fit, MY25 and Y2019 have similar model errors (Figs. 3b,d), although their model errors in the first-round plane wave analysis are very different. It is because the spatial bandpass filter in step 2 can significantly suppress nontidal noise. In summary, thanks to the new mapping technique, mode-1 M_2 internal tides can be constructed using the yearly altimeter data in 2019.

3. Results

a. *Internal tide models*

The three internal tide models Y2019, Y2019test, and MY25 are shown in Fig. 4. Shown are their SSH amplitudes in logarithmic scale. Figure 4 shows that the three models have very similar spatial patterns. All of them show that strong M_2 internal tides occur around the Hawaiian Ridge, in the western Pacific Ocean, in the Madagascar–Mascarene region, and around the French Polynesian Ridge (Ray and Zaron 2016; Zhao et al. 2016). They all have multiwave interfered spatial patterns. Note that recent internal tide models developed using different mapping techniques become more and more similar (Zaron 2019; Zhao 2021). It is hard to tell their differences in the multiwave superimposed fields.

A comparison of altimetric and moored internal tides has been conducted in a previous study (Zhao et al. 2016). Approximately 2200 historical moorings are examined and 80 moorings are qualified for extracting internal tides. The amplitude and phase of internal tides are compared, respectively (see their Fig. 11). It has been concluded that the altimetric and moored results are in fair agreement. Their differences are understandable for the following reasons: 1) Altimetric internal tides are 20–25-yr-coherent components, but moored internal tides are 0.5–2-yr-coherent components; 2) altimetric internal tides are spatially smoothed in a fitting window, but moored internal tides are measured at fixed sites; 3) altimetric internal tides can resolve multiwave interference, but moored internal tides are subject to multiwave interference.

b. *Decomposed internal tide models*

Each of the three internal tide models has been decomposed into four components by propagation direction. There are five waves of different propagation directions at each point. The five waves are determined in the second-round plane wave analysis. Taking advantage of these predetermined waves, it is straightforward to decompose one internal tide model into multiple components (Zhao 2019, 2020, 2021). Four components are obtained in this study. The northward and southward components contain waves falling in directional ranges of 30°–150° and 210°–330°, respectively. The eastward and westward components contain waves in 330°–30° and 150°–210°, respectively. The decomposed internal tide components are shown in Fig. 4. The results reveal long-range internal tidal beams, which have been observed and discussed previously (Zhao et al. 2016; Zhao 2019).

Figure 4 shows that Y2019 and Y2019test have almost the same southward and northward components. However, Y2019test underestimates the eastward and westward components. As explained above, the underestimation is caused by the along-track high-pass filter used in mapping Y2019Test. Figure 4 also shows that Y2019 and MY25 have almost the same components in all directional ranges. Y2019 has relatively larger SSH amplitudes than MY25. A detailed comparison of Y2019 and MY25 will be given in section 5. This paper replaces along-track high-pass filter with mesoscale correction, because the latter can yield better eastward and westward components. Nevertheless, along-track high-pass filtering is still useful in mapping southward and northward internal tides.

c. *Model evaluation*

These internal tide models are evaluated using independent altimeter data. There are five altimetry missions in 2018: *Sentinel-3A*, *Jason-3*, *Haiyang-2A*, *CryoSat-2*, and *SARAL*/AltiKa. The altimeter data in 2018 are not used in constructing these models. The evaluation method has been presented in previous studies (Ray and Zaron 2016; Zhao 2016b; Zaron 2019; Zhao 2019). For each SSH measurement of known time and location, the internal tide signal is predicted using the model under evaluation, and subtracted from the raw data. The variance reduction is the difference before and after the internal tide correction. All SSH measurements in 2018 are processed in the same way. In the end, the variance reductions are binned into half-overlapping $2° \times 2°$ windows on a regular grid of 1° longitude × 1° latitude.

Figure 5 shows variance reductions obtained by the three models. All models cause positive variance reduction in the ocean, indicating that they are overall robust. One can see that large variance reductions are usually associated with strong internal tides such as around the Hawaiian Ridge, the Polynesian Ridge, and the northwest Pacific. In addition, positive variance reductions can be seen throughout the Atlantic Ocean. The global mean variance reductions for Y2019, Y2019test, and MY25 are 17.8, 14.5, and 19.0 mm^2, respectively. Y2019test performs poor: its variance reduction is 3.3 mm^2 less than Y2019 (or 18%). Differences between variance reductions (Figs. 5d,f) also show that Y2019test is the worst of the three models. As discussed earlier, the poor performance of Y2019test is because it underestimates eastward and westward components.

Y2019 reduces 1.2 mm^2 less variance than MY25 (or 6%). It mean that MY25 is a little better than Y2019 overall. However, their differences have both negative and positive values in the ocean (Fig. 5e). It suggests that the model performance (i.e., variance reduction) is a function of location. Figure 5e

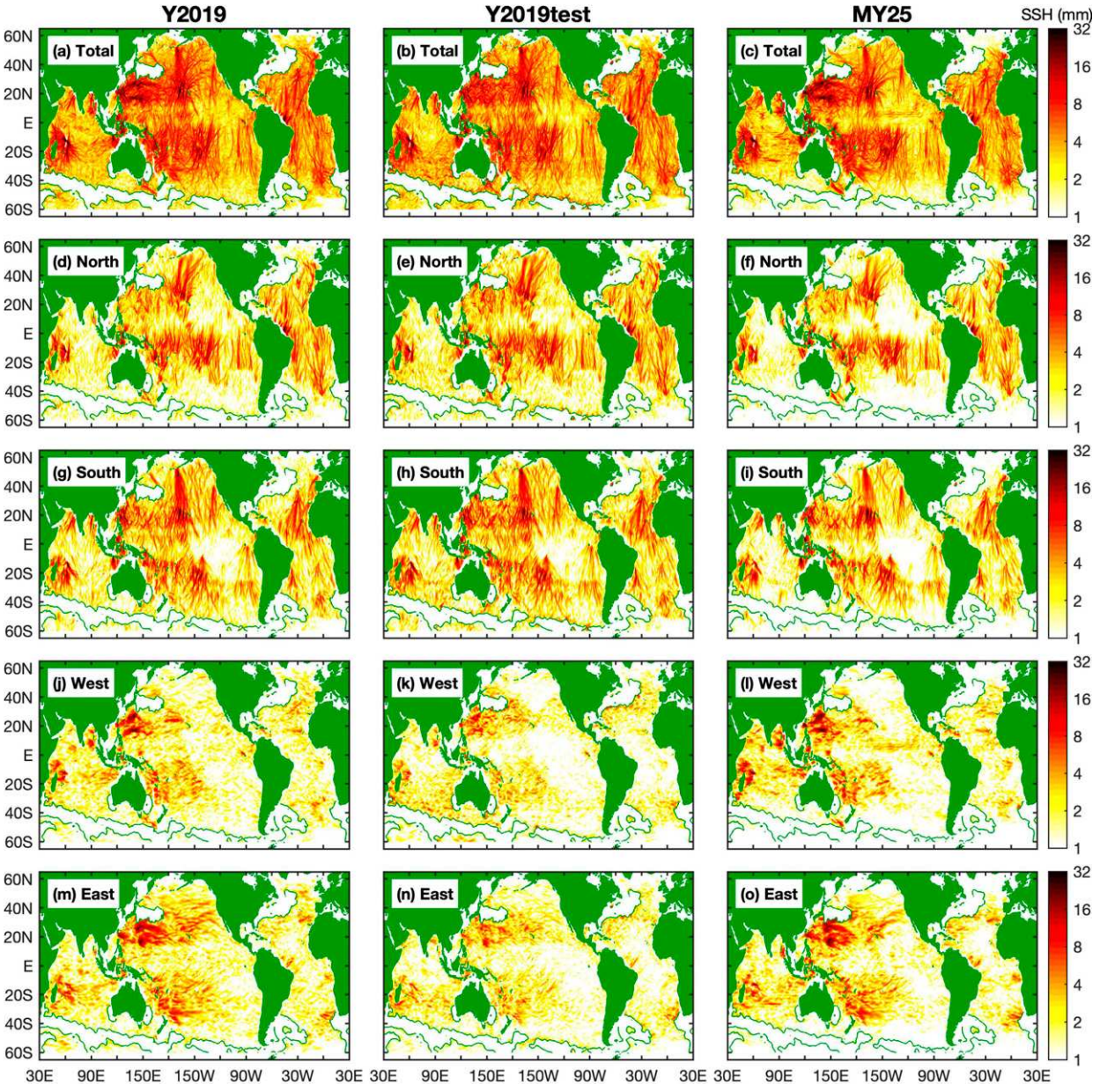

FIG. 4. Mode-1 M_2 internal tides and decomposed components. (left) Y2019. (center) Y2019test. (right) MY25. (a)–(c) Total field. (d)–(f) Northward components (30°–150°). (g)–(i) Southward components (210°–330°). (j)–(l) Westward components (150°–210°). (m)–(o) Eastward components (330°–30°). Internal tides in regions of strong currents are discarded (green contours). All three models have almost the same southward and northward components, but Y2019test underestimates the eastward and westward components.

shows that Y2019 works worse in the western Pacific Ocean and the Indian Ocean, but better in the eastern Pacific Ocean and the Atlantic Ocean. This spatial feature may be partly caused by the interannual variations of internal tides (section 5).

4. Internal tides from fewer altimetry missions

This section examines internal tide models constructed using fewer altimetry missions. The motivation question is whether mode-1 M_2 internal tide models can be constructed when there are fewer altimetry missions in one given year. To answer this question, M_2 internal tide models are mapped using altimeter data from fewer missions following the same mapping procedure. Two cases are studied here. In the first case, all altimetry missions except for *Jason-3* are used. This case is examined because the *Jason-3* ground tracks have intertrack intervals (315 km) much wider than the fitting window (Fig. 1a). In the second case, only the three nonrepeat altimetry missions (*CryoSat-2*, *Haiyang-2A*, and *SARAL*/AltiKa) are used. The two models are constructed following

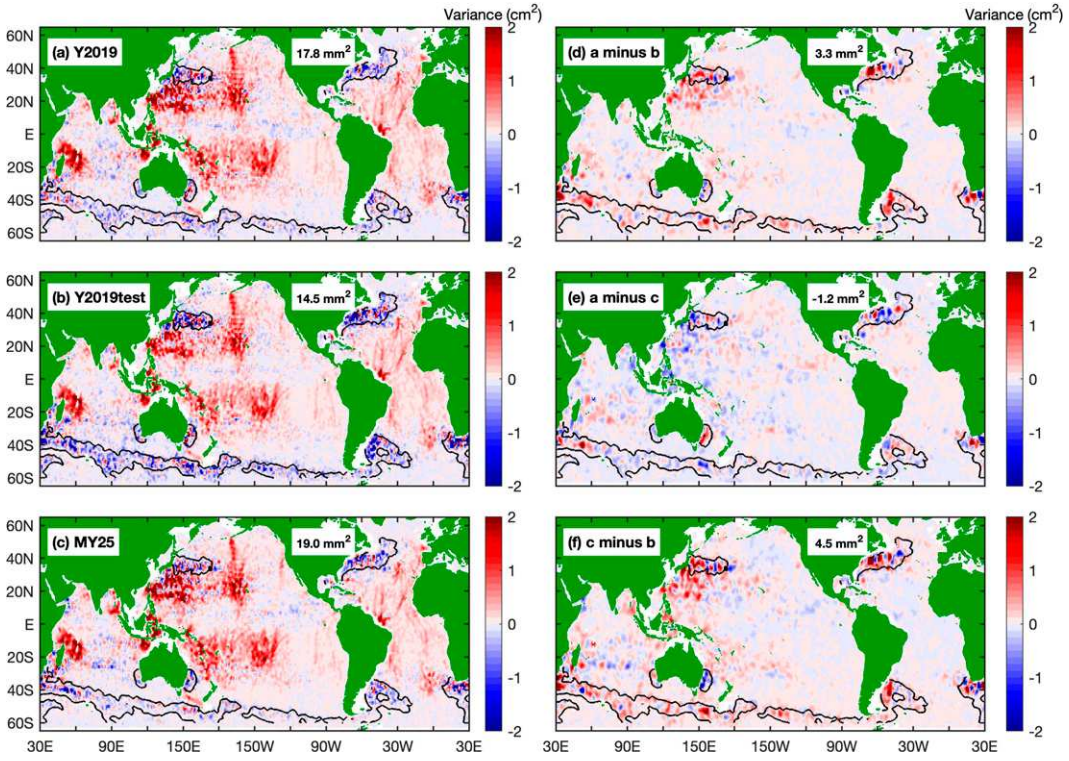

FIG. 5. Model evaluation using independent altimeter data in 2018. (left) Variance reductions obtained in making internal tide correction using three internal tide models. (right) Variance reduction differences. Black contours indicate regions of strong currents. Numbers are global mean variance reductions (excluding regions of strong currents).

the same procedure and using the same parameters. The resultant internal tide models are labeled Y2019-5m and Y2019-3m, indicating that they are from five and three altimetry missions, respectively. For comparison with Y2019, these two models are also evaluated using independent altimeter data in 2018 by the same method. Figure 6 shows the three internal tide models and their respective variance reduction maps.

Y2019 and Y2019-5m are compared first. They have similar spatial patterns, with a correlation coefficient as high as 0.97. On average, the SSH amplitude in Y2019-5m is 0.13 mm larger than Y2019, which is much lower than model noise (Fig. 3). Their global mean model variances are 24.0 and 24.4 mm^2, respectively, with a difference of 0.4 mm^2 or 1.6%. Their global mean variance reductions are 17.8 and 17.4 mm^2, differing by 0.4 mm^2 or 2%. All these numbers suggest that Y2019 and Y2019-5m are two internal tide models of same quality. One can conclude that the M_2 internal tide model can be constructed using five altimetry missions (without *Jason-3*).

Y2019-3m has a relatively poor quality. The correlation coefficient between Y2019 and Y2019-3m is 0.90, suggesting that they have similar spatial patterns. Y2019-3m has a global mean model variance of 29.0 mm^2, about 5 mm^2 (or 20%) larger than Y2019. But its variance reduction is 13.3 mm^2, about 4.5 mm^2 (or 25%) lower than Y2019. These numbers suggest that Y2019-3m has larger model noise, because model noise increases model variance, but does not help reduce variance in independent data. The poor quality of Y2019-3m is due to its short data record merged from only three altimetry missions. Its quality can be improved by using a larger fitting window. This strategy has been employed in Zhao (2016a).

Six internal tide models are mapped from the 2019 three-mission data using fitting windows of 160, 210, 225, 250, 275, and 300 km, respectively. By using larger windows, more independent altimeter data are involved in each fitting window; therefore, model noise can be suppressed. The same mapping procedure and parameters are used, expect for window size in the first-round plane wave analysis. All the resultant models have similar patterns to Y2019-3m as shown in Fig. 6e. Similarly, they all are evaluated using independent altimeter data. Their model variances and variance reductions are calculated and shown in Fig. 7. Figure 7a shows that the model variance decreases with increasing window size; however, Fig. 7b shows that the variance reduction increases with increasing window size. The results suggest that model noise is reduced by larger fitting windows. The model mapped in 275 km × 275 km windows has almost the same model variance (about 24 mm^2) as Y2019 mapped in 160 km × 160 km windows (Fig. 6). But its variance reduction (Fig. 7b, 14.8 mm^2) is lower than Y2019 (Fig. 6b, 17.8 mm^2). It means that the short data record from three altimetry missions cannot be fully compensated for by using larger windows. It implies that more concurrent altimetry missions are needed to better observe internal tides.

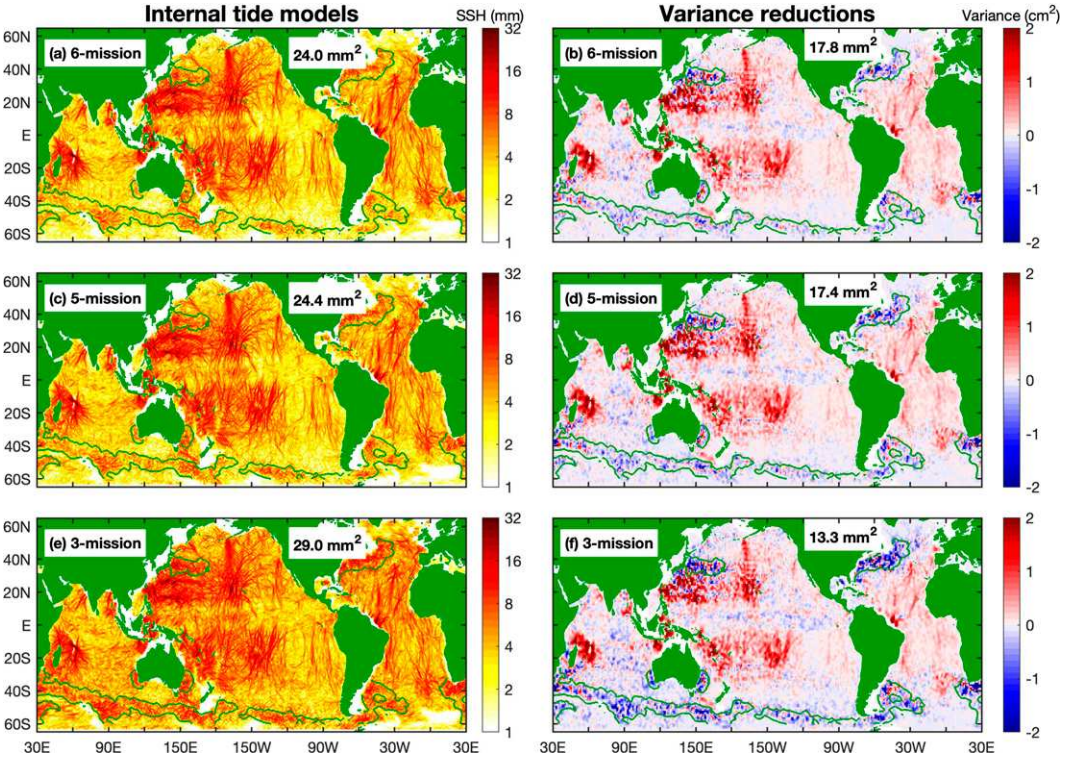

FIG. 6. Internal tide models constructed using different altimetry missions in 2019. (left) Internal tide models. (right) Variance reductions obtained in making internal tide correction to altimeter data in 2018. (a),(b) Six altimetry missions (Y2019). (c),(d) Five altimetry missions without *Jason-3* (Y2019-5m). (e),(f) Three nonrepeat altimetry missions *CryoSat-2*, *Haiyang-2A*, and *SARAL*/AltiKa (Y2019-3m). All models are constructed following the same procedure and using the same parameters (Table 2). Green contours indicate regions of strong currents. Numbers are global mean model variances or variance reductions (excluding regions of strong currents).

In summary, the M_2 internal tide model can be constructed using five or six altimetry missions. The model from three altimetry missions is poor; however, its quality can be improved by using larger fitting windows. The quality of the resultant model increases with the number of concurrent altimetry missions available. The analysis of three different datasets in 2019 confirms that both exact-repeat and nonrepeat missions can be used for mapping internal tides, thanks to the new mapping technique.

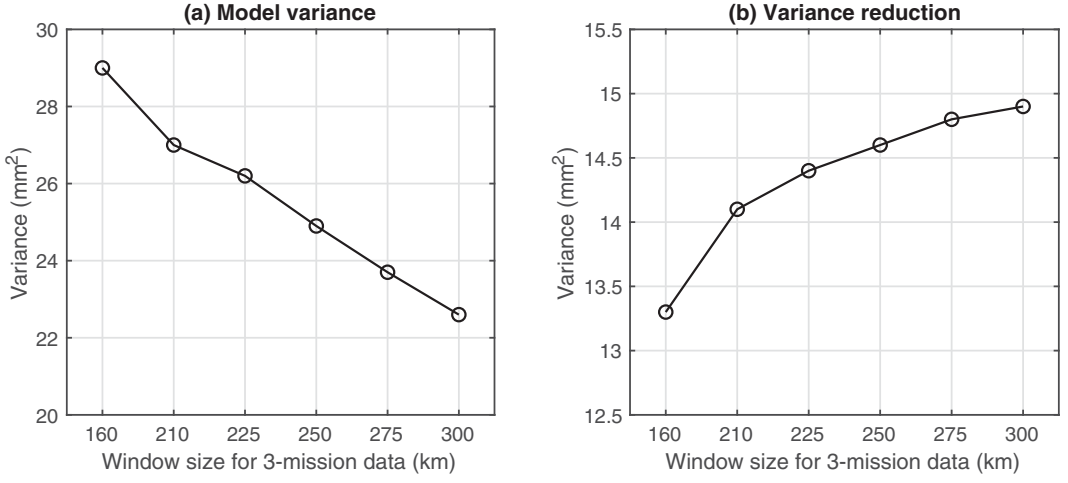

FIG. 7. Six internal tide models are constructed using the 2019 three-mission data in different fitting windows. (a) Model variance. (b) Variance reduction. The model mapped in 160 km × 160 km windows is shown in Fig. 4e. Other models have similar spatial patterns (not shown).

5. Interannual variability of internal tides

This work has been motivated to study the interannual variability of internal tides from yearly subsetted satellite altimeter data. In this section, the interannual variability of internal tides is confirmed by significant phase and amplitude differences between Y2019 and MY25. In addition, the southward internal tides from Amukta Pass (52°N, 190°E) are used to demonstrate that the interannual variations of internal tides should be interpreted along long-range internal tidal beams.

a. Phase differences

The phase differences between Y2019 and MY25 are calculated point by point. Afterward, the pointwise phase differences are smoothed by 11-point (2°) running mean along both longitude and latitude. Figure 8a shows the resultant phase differences for the total internal tide field. Both positive and negative values can be seen. In this study, positive and negative phase differences mean that M_2 internal tides travel faster and slower in Y2019 than in MY25, respectively. Positive phase differences are in the Atlantic, western Indian, and eastern Pacific Oceans. Negative phase differences are in the western Pacific and eastern Indian Oceans. The absolute values of phase differences may be greater than 90° in some regions. The phase differences are spatially coherent. These features suggest that the phase differences are caused by the interannual variability of internal tides, not by random model errors (Zhao 2016a,b).

The phase differences can be examined using the decomposed northward (30°–150°) and southward (210°–330°) components (Fig. 4). Following the same method above, the phase differences between Y2019 and MY25 are calculated for both components (Figs. 8b and 8c). For simplicity, the phase differences for the noisier eastward and westward components are not discussed here. The Greenwich 0° cophase charts are shown to indicate the propagation direction of internal tides. The intervals between two neighboring cophase lines are one wavelength. They show that internal tides propagate from well-known major generation sites.

The phase differences revealed by the northward and southward components are consistent with those in the total field. They all show negative phase differences in the western Pacific and eastern Indian Oceans, and positive phase differences in the eastern Pacific, western Indian, and Atlantic Oceans. Figures 8b and 8c give a clear picture of the phase differences. One important feature is the change (increase or decrease) of phase differences along long-range internal tidal beams. For example, along the southward internal tides from Amukta Pass (52°N, 190°E), the phase differences increase with propagation (see section 5d). In the same region, the northward internal tides from the Hawaiian Ridge also increase in phase difference (Fig. 8b). They have negative phase differences in the near field (blue) and positive values in the far field (red). On the contrary, the southward Hawaiian internal tides have negative phase differences all the way (Fig. 8c). Negative phase differences can be clearly seen in the Bay of Bengal and the Indonesian Seas. While positive phase differences are dominant in the Southern Ocean. The changes

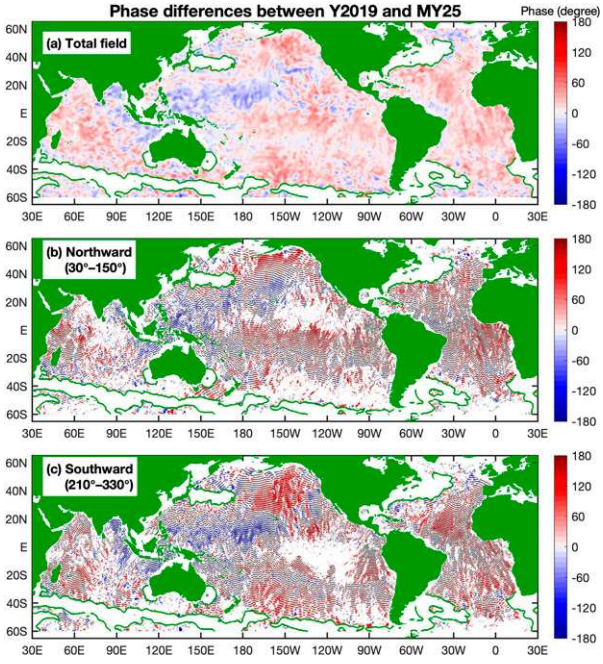

FIG. 8. Phase differences between Y2019 and MY25. Positive and negative values mean that internal tides in Y2019 travel faster and slower, respectively. (a) Total field. (b) Northward component (30°–150°). (c) Southward component (210°–330°). Shown are pointwise differences smoothed by two-dimensional 11-point running mean. Green contours indicate regions of strong currents. In (b) and (c), internal tides with SSH amplitudes < 1 mm or in regions of strong currents are not shown. Black lines are Greenwich 0° cophase charts.

of phase difference are mainly caused by different propagation speeds of internal tides during these two time periods. As explained above, positive and negative phase differences mean internal tides travel faster and slower in Y2019, respectively. The southward internal tides from the Lombok Strait have negative phase differences, which means that internal tides have slower speeds in 2019. Information on ocean stratification are inferred from phase differences (Zhao 2016a).

b. Amplitude differences

The amplitude differences between Y2019 and MY25 are calculated following the same way. Figures 9a–c show the amplitude differences for the total field, the northward and southward components, respectively. Here positive and negative values mean that Y2019 have larger and smaller SSH amplitudes, respectively. The results show that Y2019 has larger SSH amplitudes than MY25 in most of the ocean (red patches). This feature is consistent with the fact that MY25 is a 25-yr-coherent model and Y2019 is a 1-yr-coherent model. Previous studies show that the SSH amplitudes of internal tides decrease with the increasing length of time window (Dushaw 2015; Zaron 2017).

Negative SSH amplitude differences are observed in some regions including the South China Sea, in the Indonesian Seas, in the Tasman Sea, to the south of the Lombok Strait,

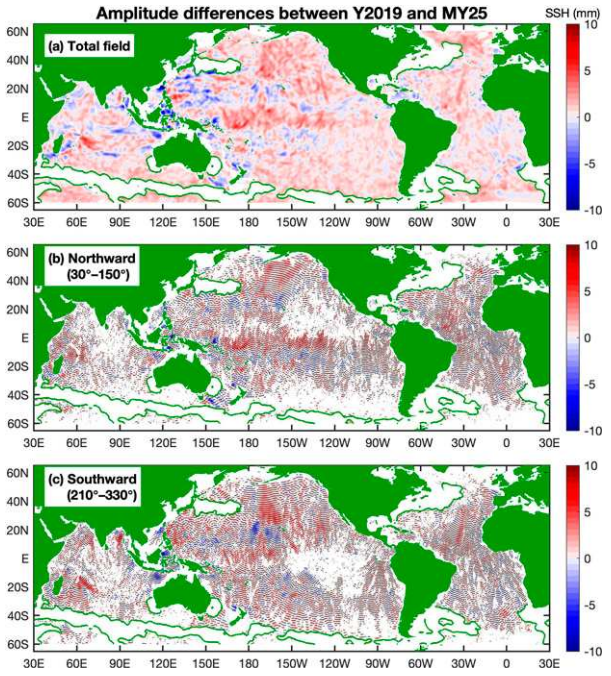

FIG. 9. As in Fig. 8, but for amplitude differences between Y2019 and MY25.

and to the south of Hawaii. This feature confirms the interannual variations of mode-1 M_2 internal tides. The differences are real signals, because 1) Y2019 and MY25 are constructed using same mapping parameters, and 2) their model errors are much lower (<1 mm). The southward M_2 internal tides from the Lombok Strait are about 5 mm lower (compared to 10 mm in MY25), which suggests that the barotropic-to-baroclinic tidal conversion in the Lombok Strait is weaker in 2019. Also, the southward radiation of internal tides from the Hawaiian Ridge is weaker in 2019. These changes may be caused by time-varying ocean stratification, mesoscale eddies, and background currents (Liu et al. 2019; Löb et al. 2020; Shakespeare 2020).

c. *Internal tide energy*

The depth-integrated internal tide energy E is calculated from the SSH amplitude η following $E = (1/2)E_n\eta^2$, where E_n is a transfer function from η to E. It is a function of tidal frequency, latitude, mode number, ocean stratification, and ocean depth. The global map of E_n for mode-1 M_2 internal tides has been computed (Zhao et al. 2016). There are five internal tidal waves at each grid point. Their energies are respectively calculated and the sum gives the internal tide energy at this grid point. The globally integrated internal tide energy is also calculated following Zhao et al. (2016). In the calculation, the decrease in the spheric area with increasing latitude is taken into account. The results show that the global energies in Y2019 and MY25 are 57 and 42 PJ (1 PJ = 10^{15} J), respectively. The energy in Y2019 is 15 PJ larger than that in Y2019 (~30%), which is reasonable, because Y2019 and MY25 represent the 1-yr-coherent and 25-yr-coherent internal tides, respectively. However, the author cautions that the yearly model from six concurrent missions contains larger model errors, particularly at high latitudes. For comparison, Zaron (2019) estimates a global energy of 44 PJ using the same 25 years of satellite data. The good agreement (44 and 42 PJ) confirms the above calculation procedure. Y2019 is closer to an estimate of 86.2 PJ in the 1/25° Hybrid Coordinate Ocean Model (HYCOM) simulation (Buijsman et al. 2020).

d. *Along-beam propagation*

The propagation of internal tides should be studied along long-range internal tidal beams. One example is given in this section. Figure 10 shows the southward internal tides from Amukta Pass (52°N, 190°E). The internal tidal beam has been separated by propagation direction. Figures 10a and 10b show the internal tidal beam in Y2019 and MY25, respectively. Y2019 has larger SSH amplitudes. For both cases, their Greenwich 0° cophase lines are shown. Figure 10c shows their phase differences. As mentioned earlier, their phase differences increase southward with propagation. Figure 10d shows the cross-beam median phase difference as a function of latitude. It shows that the phase difference increases from 0° in the near field to 60° in the far field. The 60° phase change is equivalent to ≈2 h in time. The total travel time from 51° to 30°N is ≈185 h (15 M_2 cycles). Thus, the percentage change along the beam is 1.1%. Note that the 1.1% change in speed is barely detectable by pointwise measurements (moorings, Argos). Fortunately, the weak signal is amplified with internal tide propagation. In the far field 2500 km away, it is amplified by 15 times, and can be unambiguously detected. It exemplifies how to detect small perturbations in ocean stratification by long-range internal tides. The author suggests that the percentage change of internal tide speed should be calculated along individual internal tidal beams. Their depth-integrated energy fluxes are calculated following Zhao et al. (2016), who have constructed a transfer function from SSH amplitude to energy flux. The same transfer function is used for Y2019 and MY25, neglecting a possible change with ocean stratification. Figures 10e and 10f show the resultant energy fluxes. It is obvious that the Y2019 fluxes are larger than the MY25 fluxes, consistent with their different SSH amplitudes.

Their cross-beam integrated energy fluxes are shown in Fig. 10g. It shows that Y2019 and MY25 have largest energy fluxes of 1.7 and 0.9 GW (1 GW = 10^9 W), respectively. In the near field (gray zone), the underestimation of energy fluxes is due to the narrowness of Amukta Pass compared to the fitting windows of 160 km. In the far field, their energy fluxes are 0.9 and 0.5 GW, respectively. Both dissipate about half of their energy over the 2500-km-long propagation. It means that Y2019 and MY25 have the same decay rate. Importantly, the energy flux in Y2019 is 2 times larger than in MY25, because they are the 1-yr-coherent and 25-yr-coherent models, respectively. There are more than 100 internal tidal beams in the global ocean (Fig. 4). Along each beam, propagation speed and energy flux can be studied as such. Their interannual changes can be quantified and correlated with global warming and climate changes.

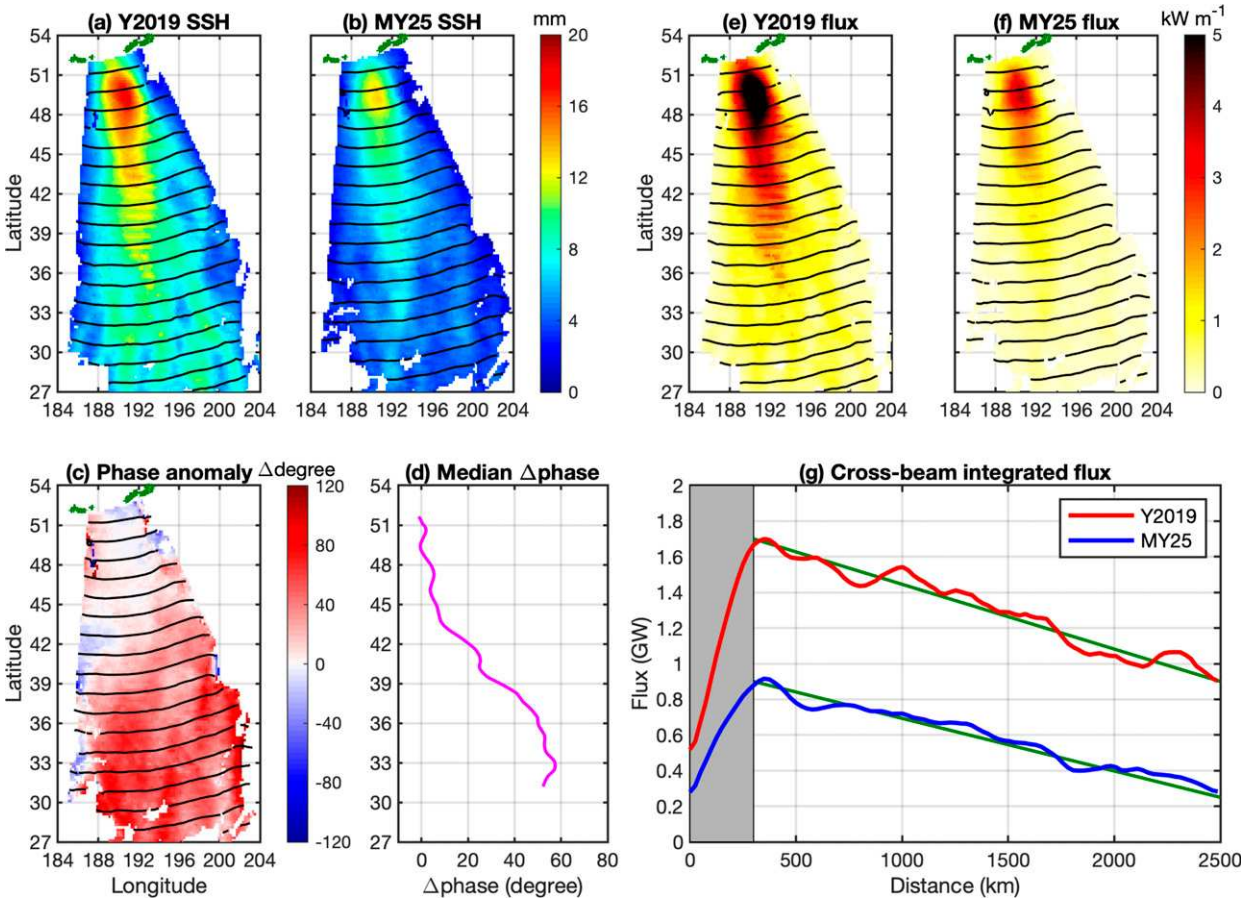

FIG. 10. Southward M_2 internal tides from Amukta Pass (52°N, 190°E). (a) Y2019 SSH amplitude. (b) MY25 SSH amplitude. (c) Phase anomaly of Y2019 with respect to MY25. Positive values mean that internal tides travel faster in Y2019. (d) Median phase anomaly as a function of latitude, showing that the phase anomaly increases from 0° in the near field to 60° in the far field. Black lines are Greenwich 0° cophase charts. (e) Y2019 energy flux. (f) MY25 energy flux. (g) Cross-beam integrated energy fluxes as a function of propagation distance. The energy flux in Y2019 is about twice that in MY25.

6. Application to other years

This new mapping technique has been applied successfully to other years. This section discusses the internal tide models in 2017 and 2018. There are six concurrent altimetry missions in 2017. They are *CryoSat-2*, *Haiyang-2A*, *Jason-2* (only 2 months long), *Jason-3*, *SARAL*/AltiKa, and *Sentinel-3A* (Abdalla et al. 2021). There are five concurrent altimetry missions in 2018. They are *CryoSat-2*, *Haiyang-2A*, *Jason-3*, *SARAL*/AltiKa, and *Sentinel-3A* (Abdalla et al. 2021). The yearly subsetted altimeter data in 2017 and 2018 are preprocessed by mesoscale correction (section 2a). Then mode-1 M_2 internal tides are mapped following the same procedure and using the same parameters (section 2d). The two models are labeled Y2017 and Y2018, respectively. Internal tide models Y2017, Y2018, and Y2019 have similar spatial patterns and global mean variances (Fig. 11). Evaluation using independent altimeter data in 2020 confirms that they have similar performances in terms of variance reduction (Fig. 11).

Their phase anomalies with respect to MY25 are calculated following the same procedure (section 5a) and shown in Fig. 12. For each model, phase anomalies are also examined using its southward and northward components. Both Y2017 and Y2018 show spatially coherent patterns, confirming that the phase anomalies are real signals, instead of model errors. These models have different phase anomalies, suggesting the interannual variations of internal tides. One remarkable feature is that, in 2017, one negative-value region is in the southern central Pacific Ocean. In 2018, this region moves to the northern central Pacific Ocean. Furthermore, this negative-value region moves to the western Pacific Ocean in 2019 (Fig. 8). This feature is likely caused by large-scale ocean oscillations such as El Niño. Further examination of its driving mechanism is worthwhile but beyond the scope of this paper.

Figure 13 compares these models along the southward internal tides from Amukta Pass. Figure 13a shows their phase anomalies. It shows that phase anomalies vary from year to year. It is consistent with the observation in Fig. 12. In 2018 and 2019, the phase anomaly increases from zero in the near field to about 60° in the far field. In 2017, however, the phase anomaly does not increase much along the beam. It is

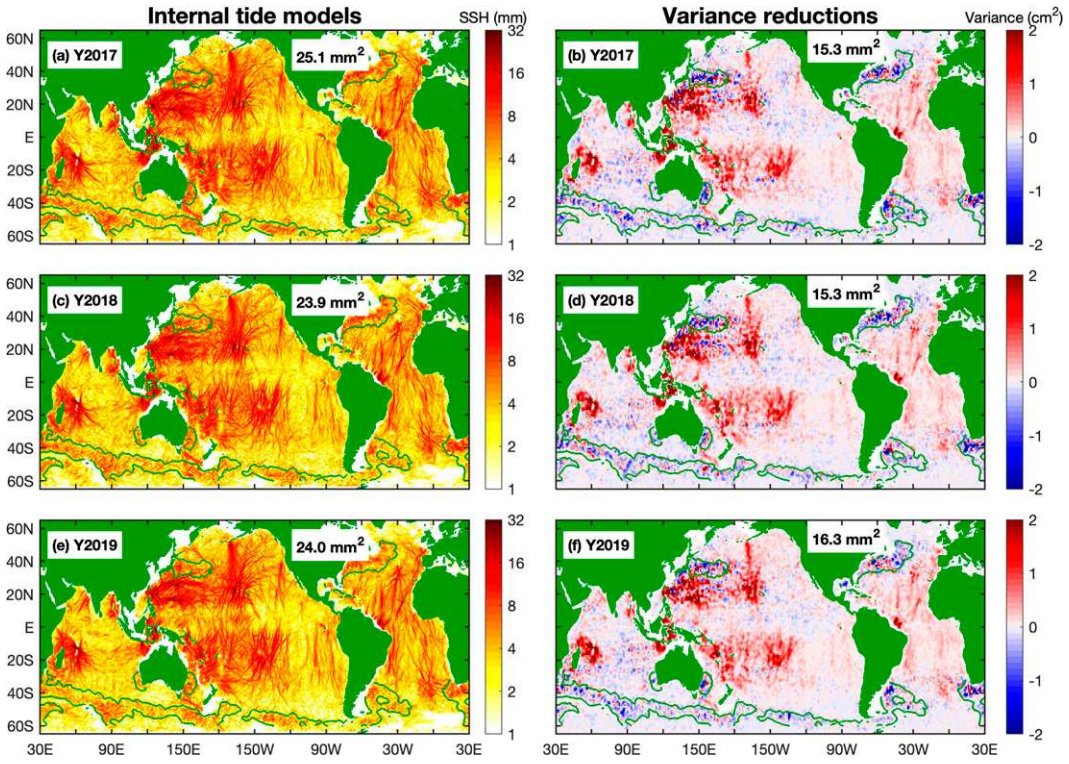

FIG. 11. Internal tide models constructed using yearly altimeter data in 2017, 2018, and 2019. (left) Internal tide models. (right) Variance reductions obtained in making internal tide correction to altimeter data in 2020. (a),(b) Y2017. (c),(d) Y2018. (e),(f) Y2019. All models are constructed following the same procedure and using the same parameters. Green contours indicate regions of strong currents. Numbers are global mean model variances or variance reductions (excluding regions of strong currents).

likely due to the interannual variation in ocean stratification and background circulation. Figure 13b shows the cross-beam integrated energy fluxes in these models. All three yearly models have energy fluxes about twice that in MY25, and decay along the beam with almost the same rate. The global energies in 2017, 2018, and 2019 are 62, 60, and 57 PJ, respectively. The author cautions that yearly models have larger model errors, because the yearly altimeter data are short.

7. Summary

It is challenging to construct robust internal tide models using yearly subsetted altimeter data. This paper addresses this challenge by developing a new mapping technique. There are six concurrent satellite altimetry missions, exact-repeat or nonrepeat, in 2019. This paper shows that yearly mode-1 M_2 internal tide model in 2019 can be constructed using the six (even five) altimetry missions. The new technique combines mesoscale correction, plane wave analysis and spatial bandpass filtering. The resultant model Y2019 is a 1-yr-coherent internal tide field. It is validated with MY25, a 25-yr-coherent field constructed using altimeter data from 1993 to 2017. The new mapping technique works well in suppressing model errors, which are as low as those in MY25. Evaluation using independent altimeter data confirms that Y2019 reduces slightly less variance (~6%) than MY25. Significant interannual variations of internal tides are revealed by comparing Y2019 and MY25.

This work shows that mode-1 M_2 internal tides can be extracted from five or six concurrent altimetry missions in one given year. This achievement is attributed to three indispensable steps in the new mapping technique. 1) Plane wave analysis suppresses model errors by using more independent data in one fitting window. It utilizes altimeter data from both exact-repeat and nonrepeat missions. It also decomposes internal tide waves into multiple waves of different propagation directions. 2) The spatial bandpass filter is indispensable in suppressing model noise. Its role can be seen by comparing internal tides obtained in the first-round and second-round plane wave analysis. 3) Previous along-track high-pass filtering yields correct southward and northward internal tides, but underestimates westward and eastward internal tides. Mesoscale correction is employed to remove mesoscale signals without harming internal tides in all propagation directions.

Comparing Y2019 and MY25 reveals that mode-1 M_2 internal tides are subject to significant interannual variability in both amplitude and phase. The interannual variations of internal tides are a function of location. The interannual variations of internal tides can be better studied using the decomposed internal tide components by propagation direction. In

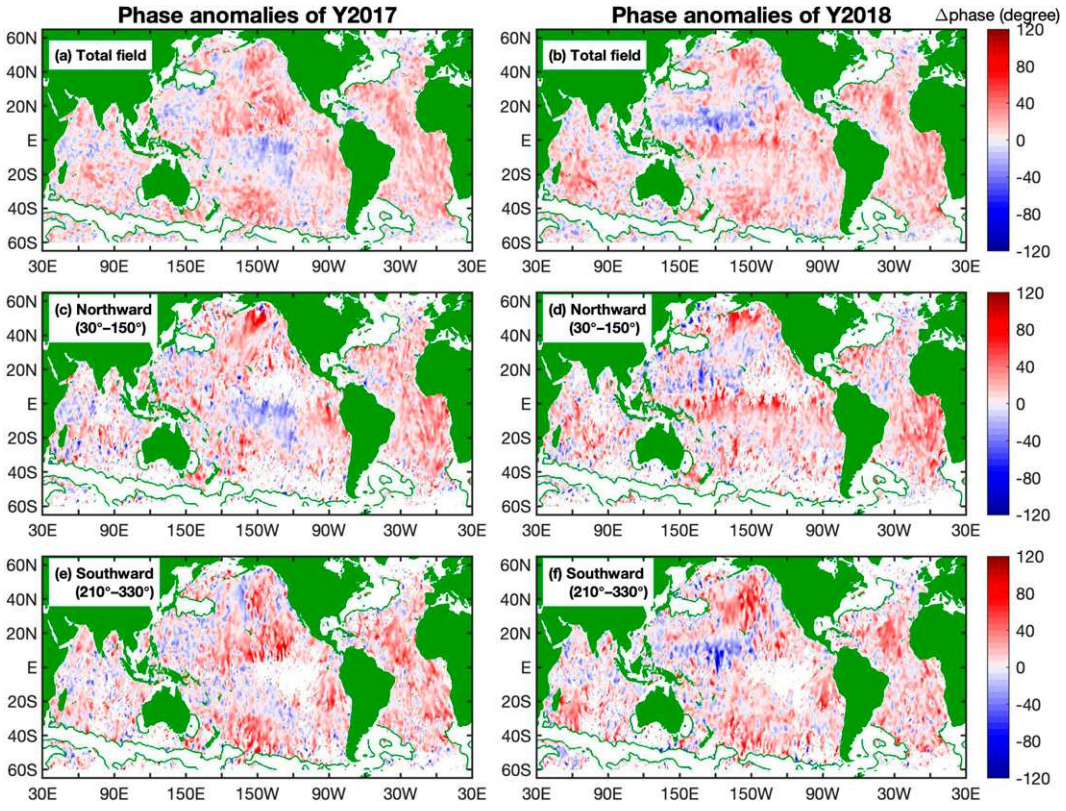

FIG. 12. Phase anomalies of (a) Y2017 and (b) Y2018 with respect to MY25. (a),(b) The total field. (c),(d) The northward component (30°–150°). (e),(f) The southward component (210°–330°). Green contours indicate regions of strong currents. Internal tides with SSH amplitudes < 1 mm or in regions of strong currents are not shown.

Y2019, internal tides travel faster in the Atlantic, eastern Pacific, and western Indian Oceans, and travel slower in the western Pacific and eastern Indian Oceans. In particular, the propagation and energetics of internal tides should be interpreted along more than 100 long-range internal tidal beams. For example, along the southward internal tidal beam from Amukta Pass, the energy flux in Y2019 is twice that in MY25 and the propagations speed is about 1.1% faster.

This mapping technique has been applied successfully to other years. The yearly internal tide models in 2017 and 2018

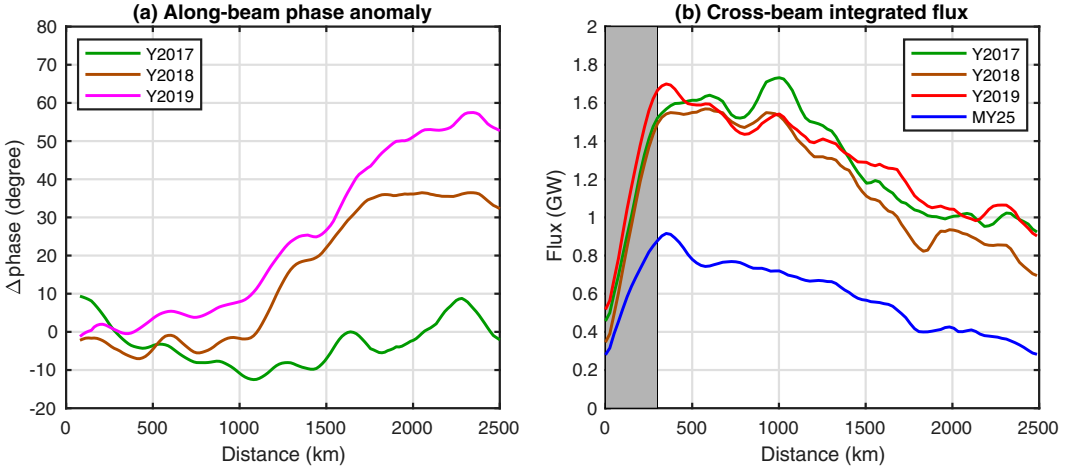

FIG. 13. (a) Phase anomalies along the southward internal tidal beam from Amukta Pass. (b) Cross-beam integrated energy flux. See Fig. 10 for the beam location.

are shown as examples. There are six and five concurrent altimetry missions in 2017 and 2018, respectively. The phase anomalies in 2017, 2018, and 2019 have different spatial patterns, suggesting the interannual variations of internal tides caused by large-scale ocean changes. It is expected that the interannual variations of internal tides can be quantified using yearly internal tide models from satellite altimetry.

Acknowledgments. This work was supported by the National Aeronautics and Space Administration (NASA) via Projects NNX17AH57G and 80NSSC18K0771, and the National Science Foundation (NSF) via Project OCE1947592. The author thanks three anonymous reviewers for their constructive comments.

Data availability statement. The satellite altimetry along-track data and gridded mesoscale fields were downloaded from the Copernicus Marine Environment Monitoring Service (http://marine.copernicus.eu, accessed 12 April 2021). The *World Ocean Atlas 2018* is produced and made available by NOAA National Oceanographic Data Center (https://www.nodc.noaa.gov/OC5/woa18/, accessed 1 May 2020). The M_2 internal tide model mapped in this study can be downloaded from https://doi.org/10.6084/m9.figshare.19395230.v1.

REFERENCES

Abdalla, S., and Coauthors, 2021: Altimetry for the future: Building on 25 years of progress. *Adv. Space Res.*, **68**, 319–363, https://doi.org/10.1016/j.asr.2021.01.022.

Alford, M. H., J. A. MacKinnon, Z. Zhao, R. Pinkel, J. Klymak, and T. Peacock, 2007: Internal waves across the Pacific. *Geophys. Res. Lett.*, **34**, L24601, https://doi.org/10.1029/2007GL031566.

Arbic, B., J. Richman, J. Shriver, P. Timko, E. Metzger, and A. Wallcraft, 2012: Global modeling of internal tides within an eddying ocean general circulation model. *Oceanography*, **25** (2), 20–29, https://doi.org/10.5670/oceanog.2012.38.

Buijsman, M. C., B. K. Arbic, J. G. Richman, J. F. Shriver, A. J. Wallcraft, and L. Zamudio, 2017: Semidiurnal internal tide incoherence in the equatorial Pacific. *J. Geophys. Res. Oceans*, **122**, 5286–5305, https://doi.org/10.1002/2016JC012590.

——, and Coauthors, 2020: On the interplay between horizontal resolution and wave drag and their effect on tidal baroclinic mode waves in realistic global ocean simulations. *Ocean Modell.*, **152**, 101656, https://doi.org/10.1016/j.ocemod.2020.101656.

Carrere, L., and Coauthors, 2021: Accuracy assessment of global internal tide models using satellite altimetry. *Ocean Sci.*, **17**, 147–180, https://doi.org/10.5194/os-17-147-2021.

de Lavergne, C., and Coauthors, 2020: A parameterization of local and remote tidal mixing. *J. Adv. Model. Earth Syst.*, **12**, e2020MS002065, https://doi.org/10.1029/2020MS002065.

Dibarboure, G., A. Lamy, M.-I. Pujol, and G. Jettou, 2018: The drifting phase of SARAL: Securing stable ocean mesoscale sampling with an unmaintained decaying altitude. *Remote Sens.*, **10**, 1051, https://doi.org/10.3390/rs10071051.

Dushaw, B. D., 2015: An empirical model for mode-1 internal tides derived from satellite altimetry: Computing accurate tidal predictions at arbitrary points over the world oceans. University of Washington Applied Physics Laboratory Tech. Rep., 114 pp.

Egbert, G. D., and R. D. Ray, 2000: Significant dissipation of tidal energy in the deep ocean inferred from satellite altimeter data. *Nature*, **405**, 775–778, https://doi.org/10.1038/35015531.

Garrett, C., and E. Kunze, 2007: Internal tide generation in the deep ocean. *Annu. Rev. Fluid Mech.*, **39**, 57–87, https://doi.org/10.1146/annurev.fluid.39.050905.110227.

Jayne, S. R., and L. C. St. Laurent, 2001: Parameterizing tidal dissipation over rough topography. *Geophys. Res. Lett.*, **28**, 811–814, https://doi.org/10.1029/2000GL012044.

Kelly, S. M., 2016: The vertical mode decomposition of surface and internal tides in the presence of a free surface and arbitrary topography. *J. Phys. Oceanogr.*, **46**, 3777–3788, https://doi.org/10.1175/JPO-D-16-0131.1.

——, A. F. Waterhouse, and A. C. Savage, 2021: Global dynamics of the stationary M_2 mode-1 internal tide. *Geophys. Res. Lett.*, **48**, e2020GL091692, https://doi.org/10.1029/2020GL091692.

Kong, Q., F. Gao, J. Guo, L. Han, L. Zhang, and Y. Shen, 2019: Analysis of precise orbit predictions for a HY-2A satellite with three atmospheric density models based on dynamic method. *Remote Sens.*, **11**, 40, https://doi.org/10.3390/rs11010040.

Liu, K., J. Sun, C. Guo, Y. Yang, W. Yu, and Z. Wei, 2019: Seasonal and spatial variations of the M_2. *J. Geophys. Res. Oceans*, **124**, 1115–1138, https://doi.org/10.1029/2018JC014819.

Löb, J., J. Köhler, C. Mertens, M. Walter, Z. Li, J.-S. von Storch, Z. Zhao, and M. Rhein, 2020: Observations of the low-mode internal tide and its interaction with mesoscale flow south of the Azores. *J. Geophys. Res. Oceans*, **125**, e2019JC015879, https://doi.org/10.1029/2019JC015879.

Locarnini, R. A., and Coauthors, 2013: Temperature. Vol. 1. *World Ocean Atlas 2013*, NOAA Atlas NESDIS 73, 40 pp., http://data.nodc.noaa.gov/woa/WOA13/DOC/woa13_vol1.pdf.

MacKinnon, J. A., and Coauthors, 2017: Climate process team on internal wave-driven ocean mixing. *Bull. Amer. Meteor. Soc.*, **98**, 2429–2454, https://doi.org/10.1175/BAMS-D-16-0030.1.

Niwa, Y., and T. Hibiya, 2014: Generation of baroclinic tide energy in a global three-dimensional numerical model with different spatial grid resolutions. *Ocean Modell.*, **80**, 59–73, https://doi.org/10.1016/j.ocemod.2014.05.003.

Pujol, M.-I., Y. Faugère, G. Taburet, S. Dupuy, C. Pelloquin, M. Ablain, and N. Picot, 2016: DUACS DT2014: The new multi-mission altimeter data set reprocessed over 20 years. *Ocean Sci.*, **12**, 1067–1090, https://doi.org/10.5194/os-12-1067-2016.

Ray, R. D., and G. T. Mitchum, 1996: Surface manifestation of internal tides generated near Hawaii. *Geophys. Res. Lett.*, **23**, 2101–2104, https://doi.org/10.1029/96GL02050.

——, and D. A. Byrne, 2010: Bottom pressure tides along a line in the southeast Atlantic Ocean and comparisons with satellite altimetry. *Ocean Dyn.*, **60**, 1167–1176, https://doi.org/10.1007/s10236-010-0316-0.

——, and E. D. Zaron, 2011: Non-stationary internal tides observed with satellite altimetry. *Geophys. Res. Lett.*, **38**, L17609, https://doi.org/10.1029/2011GL048617.

——, and ——, 2016: M_2 internal tides and their observed wavenumber spectra from satellite altimetry. *J. Phys. Oceanogr.*, **46**, 3–22, https://doi.org/10.1175/JPO-D-15-0065.1.

Rudnick, D. L., and Coauthors, 2003: From tides to mixing along the Hawaiian Ridge. *Science*, **301**, 355–357, https://doi.org/10.1126/science.1085837.

Shakespeare, C. J., 2020: Interdependence of internal tide and lee wave generation at abyssal hills: Global calculations. *J. Phys. Oceanogr.*, **50**, 655–677, https://doi.org/10.1175/JPO-D-19-0179.1.

Vic, C., and Coauthors, 2019: Deep-ocean mixing driven by small-scale internal tides. *Nat. Commun.*, **10**, 2099, https://doi.org/10.1038/s41467-019-10149-5.

Whalen, C. B., C. de Lavergne, A. C. Naveira Garabato, J. M. Klymak, J. A. MacKinnon, and K. L. Sheen, 2020: Internal wave-driven mixing: Governing processes and consequences for climate. *Nat. Rev. Earth Environ.*, **1**, 606–621, https://doi.org/10.1038/s43017-020-0097-z.

Wingham, D. J., and Coauthors, 2006: CryoSat: A mission to determine the fluctuations in Earth's land and marine ice fields. *Adv. Space Res.*, **37**, 841–871, https://doi.org/10.1016/j.asr.2005.07.027.

Zaron, E. D., 2017: Mapping the nonstationary internal tide with satellite altimetry. *J. Geophys. Res. Oceans*, **122**, 539–554, https://doi.org/10.1002/2016JC012487.

——, 2019: Baroclinic tidal sea level from exact-repeating mission altimetry. *J. Phys. Oceanogr.*, **49**, 193–210, https://doi.org/10.1175/JPO-D-18-0127.1.

——, and G. D. Egbert, 2014: Time-variable refraction of the internal tide at the Hawaiian Ridge. *J. Phys. Oceanogr.*, **44**, 538–557, https://doi.org/10.1175/JPO-D-12-0238.1.

——, and R. D. Ray, 2018: Aliased tidal variability in mesoscale sea level anomaly maps. *J. Atmos. Oceanic Technol.*, **35**, 2421–2435, https://doi.org/10.1175/JTECH-D-18-0089.1.

Zhao, Z., 2016a: Internal tide oceanic tomography. *Geophys. Res. Lett.*, **43**, 9157–9164, https://doi.org/10.1002/2016GL070567.

——, 2016b: Using CryoSat-2 altimeter data to evaluate M_2 internal tides observed from multisatellite altimetry. *J. Geophys. Res. Oceans*, **121**, 5164–5180, https://doi.org/10.1002/2016JC011805.

——, 2019: Mapping internal tides from satellite altimetry without blind directions. *J. Geophys. Res. Oceans*, **124**, 8605–8625, https://doi.org/10.1029/2019JC015507.

——, 2020: Southward internal tides in the northeastern South China Sea. *J. Geophys. Res. Oceans*, **125**, e2020JC01654, https://doi.org/10.1029/2020JC016554.

——, 2021: Seasonal mode-1 M_2 internal tides from satellite altimetry. *J. Phys. Oceanogr.*, **51**, 3015–3035, https://doi.org/10.1175/JPO-D-21-0001.1.

——, M. H. Alford, J. B. Girton, L. Rainville, and H. L. Simmons, 2016: Global observations of open-ocean mode-1 M_2. *J. Phys. Oceanogr.*, **46**, 1657–1684, https://doi.org/10.1175/JPO-D-15-0105.1.

——, J. Wang, D. Menemenlis, L.-L. Fu, S. Chen, and B. Qiu, 2019: Decomposition of the multimodal multidirectional M_2. *J. Atmos. Oceanic Technol.*, **36**, 1157–1173, https://doi.org/10.1175/JTECH-D-19-0022.1.

Zhou, X.-H., D.-P. Wang, and D. Chen, 2015: Validating satellite altimeter measurements of internal tides with long-term TAO/TRITON buoy observations at 2°. *Geophys. Res. Lett.*, **42**, 4040–4046, https://doi.org/10.1002/2015GL063669.

Zweng, M., and Coauthors, 2013: Salinity. Vol. 2. *World Ocean Atlas 2013*, NOAA Atlas NESDIS 74, 39 pp., http://data.nodc.noaa.gov/woa/WOA13/DOC/woa13_vol2.pdf.